Acta Pharmaceutica Sinica B 2025;15(6):3243−3258



Chinese Pharmaceutical Association
Institute of Materia Medica, Chinese Academy of Medical Sciences

Acta Pharmaceutica Sinica B

www.elsevier.com/locate/apsb
www.sciencedirect.com



ORIGINAL ARTICLE

A photodynamic nanohybrid system reverses hypoxia and augment anti-primary and metastatic tumor efficacy of immunotherapy



Haitao Yuan[a,†], Xiaoxian Wang[b,†], Xin Sun[a,†], Di Gu[c,d,†], Jinan Guo[a,d,†], Wei Huang[e], Jingbo Ma[a], Chunjin Fu[a], Da Yin[a,*], Guohua Zeng[c,d,*], Ying Long[b,*], Jigang Wang[a,c,f,g,*], Zhijie Li[a,*]

[a]*Department of Cardiology, Guangdong Provincial Clinical Research Center for Geriatrics, Shenzhen Clinical Research Center for Geriatric, Shenzhen People's Hospital (The Second Clinical Medical College, Jinan University, The First Affiliated Hospital, Southern University of Science and Technology), Shenzhen 518020, China*
[b]*Department of Hyperbaric Oxygen Medicine, Shenzhen People's Hospital, The First Affiliated Hospital, Southern University of Science and Technology, Shenzhen 518020, China*
[c]*Guangdong Key Laboratory of Urology, The First Affiliated Hospital of Guangzhou Medical University, Guangzhou 510230, China*
[d]*Department of Urology, Shenzhen People's Hospital (The Second Clinical Medical College, Jinan University; The First Affiliated Hospital, Southern University of Science and Technology), Shenzhen 518020, China*
[e]*School of Chemical Engineering and Technology, Sun Yat-sen University, Zhuhai 519082, China*
[f]*State Key Laboratory of Antiviral Drugs, School of Pharmacy, Henan University, Kaifeng 475004, China*
[g]*State Key Laboratory for Quality Ensurance and Sustainable Use of Dao-di Herbs, Artemisinin Research Center, and Institute of Chinese Materia Medica, China Academy of Chinese Medical Sciences, Beijing 100700, China*

Received 19 October 2024; received in revised form 15 January 2025; accepted 20 February 2025

KEY WORDS

Photodynamic immunotherapy;
Hypoxia;
Vascular normalization;
Immunogenic cell death;

Abstract Photodynamic immunotherapy is a promising strategy for cancer treatment. However, the dysfunctional tumor vasculature results in tumor hypoxia and the low efficiency of drug delivery, which in turn restricts the anticancer effect of photodynamic immunotherapy. In this study, we designed photosensitive lipid nanoparticles. The synthesized PFBT@Rox Lip nanoparticles could produce type I/II reactive oxygen species (ROS) by electron or energy transfer through PFBT under light irradiation. Moreover, this nanosystem could alleviate tumor hypoxia and promote vascular normalization through Roxadustat.

*Corresponding authors.
E-mail addresses: szyinda@hotmail.com (Da Yin), gzgyzgh@vip.sina.com (Guohua Zeng), 13823730482@139.com (Ying Long), jgwang@icmm.ac.cn (Jigang Wang), li.zhijie@szhospital.com (Zhijie Li).
[†]These authors made equal contributions to this work.

Peer review under the responsibility of Chinese Pharmaceutical Association and Institute of Materia Medica, Chinese Academy of Medical Sciences.

https://doi.org/10.1016/j.apsb.2025.04.007
2211-3835 © 2025 The Authors. Published by Elsevier B.V. on behalf of Chinese Pharmaceutical Association and Institute of Materia Medica, Chinese Academy of Medical Sciences. This is an open access article under the CC BY-NC-ND license (http://creativecommons.org/licenses/by-nc-nd/4.0/).

Cancer therapy;
Reactive oxygen species;
Checkpoint blockades;
Tumor microenvironment

Upon irradiation with white light, the ROS produced by PFBT@Rox Lip nanoparticles *in situ* dysregulated calcium homeostasis and triggered endoplasmic reticulum stress, which further promoted the release of damage-associated molecular patterns, enhanced antigen presentation, and stimulated an effective adaptive immune response, ultimately priming the tumor microenvironment (TME) together with the hypoxia alleviation and vessel normalization by Roxadustat. Indeed, *in vivo* results indicated that PFBT@Rox Lip nanoparticles promoted M1 polarization of tumor-associated macrophages, recruited more natural killer cells, and augmented infiltration of T cells, thereby leading to efficient photodynamic immunotherapy and potentiating the anti-primary and metastatic tumor efficacy of PD-1 antibody. Collectively, photodynamic immunotherapy with PFBT@Rox Lip nanoparticles efficiently program TME through the induction of immunogenicity and oxygenation, and effectively suppress tumor growth through immunogenic cell death and enhanced anti-tumor immunity.

© 2025 The Authors. Published by Elsevier B.V. on behalf of Chinese Pharmaceutical Association and Institute of Materia Medica, Chinese Academy of Medical Sciences. This is an open access article under the CC BY-NC-ND license (http://creativecommons.org/licenses/by-nc-nd/4.0/).

1. Introduction

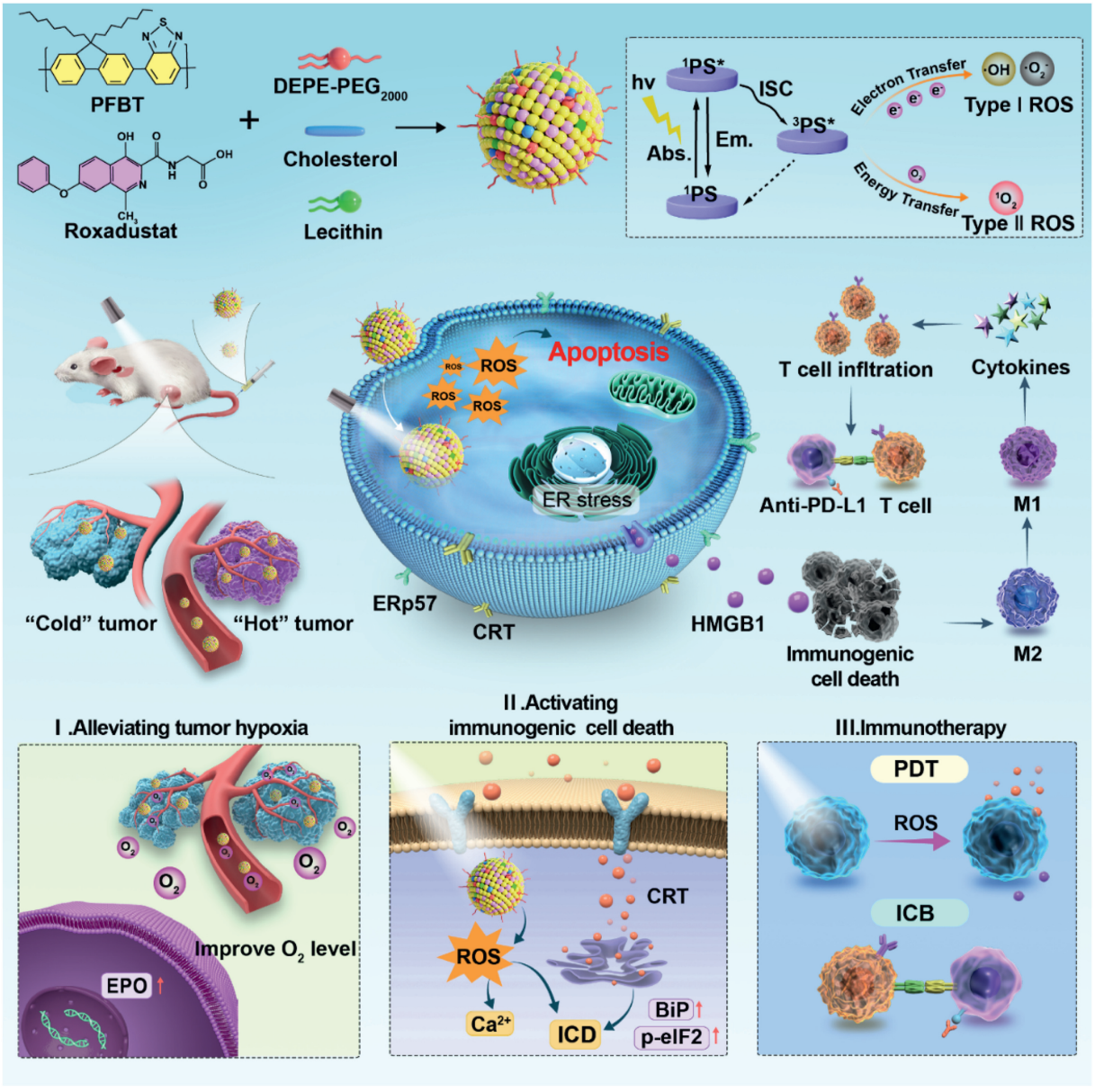
Tumor hypoxia is largely caused by an imbalance between the limited oxygen supply due to the aberrant vascular structure and the unrestrained proliferation of cancer cells[1,2]. As a fundamental characteristic of the microenvironment of solid tumors, hypoxia induces the production of a large number of antigenic factors, chemokines, and bioactive mediators, which hinders drug delivery and induces tumor cell chemoresistance, thus promoting tumor progression and metastasis[3,4]. Colorectal cancer (CRC) is one of the most common malignant tumors worldwide and is the third most diagnosed cancer[5]. Angiogenesis plays a crucial role in the occurrence and development of CRC[6]. Abnormal tumor blood vessels lead to the formation of the tumor microenvironment with low oxygen and pH, which accelerates tumor deterioration and promotes immunosuppression. Anti-angiogenesis agents such as anti-VEGF antibodies like bevacizumab have benefited patients with CRC through tumor vascular normalization and hypoxia amelioration[7,8]. Hypoxia is a prototypical characteristic of TME for most solid tumors and is highly associated with resistance to various cancer therapies such as chemotherapy, radiotherapy, and immunotherapy[9,10]. Normalized tumor vascular network could directly alleviate hypoxia and promote T cell infiltration. Alleviated hypoxia preferentially induces polarization of TAM to M1-like phenotype[11]. Besides, vessel normalization decreases the recruitment of Treg and myeloid-derived suppressor cells (MDSC)[12]. Hypoxia-induced inhibitory immune signals such as PD-L1 could be down-regulated by improved perfusion[13]. Bevacizumab, an FDA-approved humanized monoclonal antibody against VEGF, has demonstrated the functions of tumor vessel normalization to enhance the anti-tumor efficacy of immunotherapy[14,15]. Roxadustat is the first hypoxia-inducible factor prolyl hydroxylase inhibitor (HIF−PHI) used for symptomatic anemia in the clinic, which can enhance the production of erythropoietin within the physiological range and can significantly increase the hemoglobin (Hb) content of patients. Later on, it is also demonstrated that Roxadustat can normalize tumor blood vessels, improve tumor tissue perfusion, and re-oxygenated the tumor tissue[16], which is consistent with the indication of knockdown PHD (prolyl hydroxylase) in tumors[17,18]. Normalized tumor vasculature with increased vascular perfusion could potentially reduce metastasis, and restore endothelial junctions, resulting in the more efficient delivery of drugs and oxygen to the targeted tumor cells[19]. Therefore, the induction of vessel normalization has been a promising method to gain control of tumors more effectively.

Photodynamic therapy (PDT) is a new, minimally invasive cancer treatment that attracts considerable interest owing to its high spatiotemporal precision and accurate controllability[20]. Upon photoactivation, photosensitizers undergo type I (electron transfer) and type II (energy transfer) reactions that produce a large number of destructive reactive oxygen species (ROS) and thereby damage tumor cells by inducing apoptosis or necrosis, vascular destruction, and other related immune responses. The majority of the photosensitizers currently used are type II photosensitizers that mainly produce singlet oxygen ($^1O_2$). Considering that ROS production by type II photosensitizers is highly dependent on oxygen, the efficiency of this process is limited due to tumor hypoxia in TME[21]. In contrast, type I photosensitizers are more resistant to hypoxia and can fully utilize the limited amount of oxygen in the tumor microenvironment during therapy[22]. Therefore, type II photosensitizers are more suitable for use in environments with sufficient oxygen, whereas type I photosensitizers are preferentially used in anoxic environments. To establish PDT for a wide range of clinical applications, it is significant to develop photosensitizers simultaneously endowed with type I and II properties to generate high levels of ROS in solid tumors. However, due to abnormal tumor vasculature, hypoxia is an intrinsic characteristic of many malignant solid tumors. Therefore, the therapeutic effect of PDT is frequently compromised. Compared with healthy vessels, tumor vasculature is characterized by irregular structure, high tortuosity, vascular leakage, and slow flow rate[23]. These abnormal tumor vasculatures and impaired perfusion could restrict oxygen supply and drug delivery, resulting in limited PDT efficacy. At the same time, oxygen consumption and shutdown of the tumor vascular system during PDT treatment may further exacerbate tumor hypoxia, which in turn makes the treatment less effective. Thus, hypoxia caused by abnormal tumor vasculature is a major obstacle to PDT, and increasing oxygen content in tumors by normalizing abnormal tumor vasculature might be a promising strategy to improve the efficacy of PDT. In addition, PDT can also trigger immunogenic cell death (ICD) and activate immune responses for immunotherapy through the induction of macrophage polarization and T cell infiltration[24], both bolstered by tumor vessel normalization as well[25].

The endoplasmic reticulum (ER) is an indispensable cellular organelle with important biological functions[26]. When the

produced ROS damages the ER, the accumulation of misfolded proteins interferes with ER homeostasis, resulting in the ER stress[27]. Therefore, the ER could be an effective target for PDT[28]. The ER stress can result in immunogenic cell death (ICD) by promoting the release of damage-associated molecular patterns (DAMPs)[29]. Such as cell surface-exposed calreticulin (CRT) and high mobility group protein B1 (HMGB1) activate dendritic cells, ultimately enhancing the antigen presentation to T cells and invigorating the adaptive immune response[30-32]. As an attractive tumor therapeutic strategy, the induction of ICD is of great significance for activating anti-tumor immunity and producing long-term anti-tumor efficacy.

In this study, we designed photosensitive lipid nanoparticles containing poly [(9,9-dioctylfluorenyl-2,7-diyl)-alt-(benzo[2,1,3] thiadiazol-4,7-diyl)] and Roxadustat (PFBT@Rox Lip) with the properties of type I/II ROS production for PDT and proposed a new strategy to promote vessel normalization, re-oxygenate the tumor tissue, remodel the TME and achieve synergistic anti-tumor photo-immunotherapy with checkpoint blockades (Scheme 1). The use of PFBT@Rox Lip not only relieves tumor hypoxia but also promotes normalized vascular changes. Upon irradiation with white light, ROS produced by PFBT@Rox Lip *in situ* dysregulated calcium homeostasis and triggered ER stress, promoting the release of DAMPs that augment the DC antigen presentation to T cells and stimulate an effective adaptive immune response. At the same time, PFBT@Rox Lip nanoparticles induce M1 polarization of tumor-associated macrophages, increase infiltration of natural killer (NK) cells and T cells, and up-regulate the secretion of inflammatory factors, thus leading to efficient photodynamic tumor repression. Combined with PD-1 antibody, PFBT@Rox Lip



Scheme 1 Diagram of the anti-tumor mechanisms illustrating the process of the photodynamic immunotherapy that reverses hypoxia and promotes normalized vascular for tumor immunosuppression.

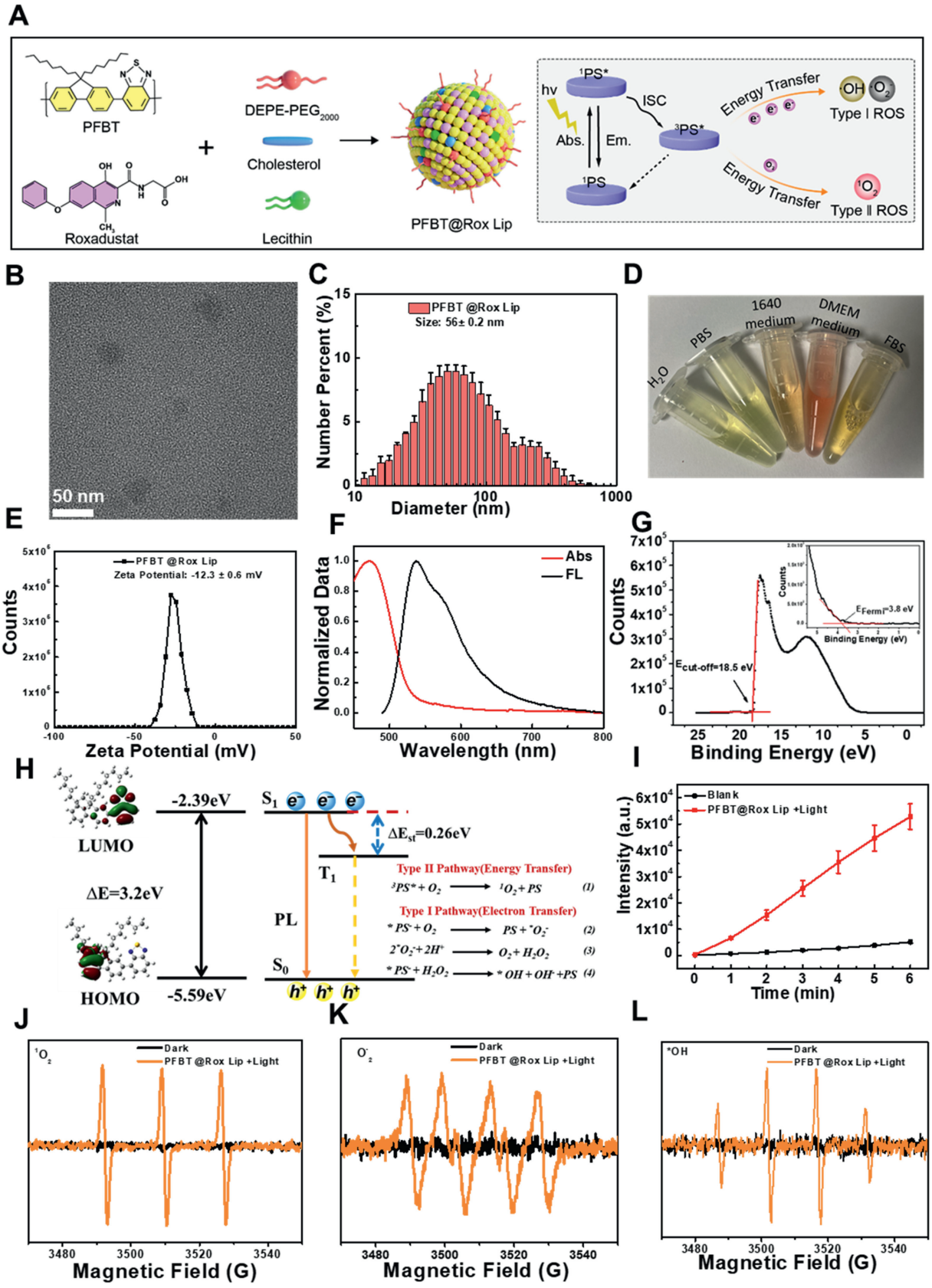


Figure 1 Characterization of PFBT@Rox Lip nanoparticles. (A) Schematic illustration of the fabrication for PFBT@Rox Lip nanoparticles. (B) TEM images of a PFBT@Rox Lip nanoparticle. scale bar = 50 nm (C) The dynamic light scattering pattern of PFBT@Rox Lip nanoparticles. (D) Images of PFBT@Rox Lip dispersed in different solvents. (E) Zeta potential of PFBT@Rox Lip nanoparticles. (F) Normalized UV−visible absorption and fluorescence emission spectra of PFBT@Rox Lip nanoparticles. (G) Ultraviolet photoelectron spectra of PFBT. (H) Mechanisms

further remarkably inhibited the primary tumor development and significantly suppressed the metastatic tumors.

2. Materials and methods

2.1. Materials

Poly[(9,9-dioctylfluorenyl-2,7-diyl)-alt-(benzo[2,1,3]thiadiazol-4,7-diyl) purchased from RuiXun Technology Co., Ltd. (Xi'an, China). 1,2-Distearoyl-sn-glycero-3-phosphoethanolamine-*N*-[methoxy(polyethylene glycol)-2000], lecithin, Cy5-DSPE-PEG_{2000} and cholesterol were from Xi'an Ruixi Biological Technology Co., Ltd. Calretinin antibody, BiP, p-eIF2α, eIF2α, β-actin and ERp57 antibody were purchased from Abcam (Shanghai, China). Cell Counting Kit-8 assay, RPMI1640 medium, and fetal bovine serum (FBS) were provided by GIBCO Invitrogen Corp. Co., Ltd. (Carlsbad, CA, USA). Paraformaldehyde (PFA) (4%), Calcein-AM/PI Double Stain Kit, and Ca^{2+} Kit were purchased from Beyotime Company Co., Ltd. (Shanghai, China). Annexin V-FITC/PI apoptosis kit was obtained from MultiSciences Co., Ltd. (Hangzhou, China). Roxadustat was obtained from MCE Co., Ltd. (Shanghai, China). Ultrapure water (18.2 MΩ; Millipore Co., USA) was used to prepare all buffers and employed in all experiments. All chemical agents were used directly without further purification.

2.2. Synthesis of PFBT@Rox Lip

Briefly, cholesterol, lecithin, DSPE-PEG_{2000}, Roxadustat and PFBT were dissolved in a mixed solution of THF solution, the optimal therapeutic dose ratio of PFBT and Roxadustat in our nanosystem is 2:1, evaporated at 40 °C to get a dry lipid film, followed by the addition of 10 mL of aqueous solution with ultrasonic hydration for 10 min.

2.3. Tracking of the internalization analysis of the PFBT@Rox Lip into cells

Cellular uptake was investigated by confocal laser scanning microscopy (CLSM). Colon26 cells were seeded onto a 24-well plate containing cover glass (1×10^4 cells in each well) and incubated overnight for adherence. Then, RPMI 1640 (0.5 mL/well) containing PFBT@Rox Lip (0.2 μg/mL) was added to the plate for 4, 8, 12 and 24 h. Finally, the cells were observed by CLSM.

2.4. Cell viability assay

Colon26 cells were seeded in 96-well plates (Corning) at a density of 8×10^3 cells per well and incubated overnight. Then cells were treated with PFBT@Rox Lip at different drug concentrations for 24 h, during which light irradiation (40 mW/cm^2 for 10 min) was treated at 12 h. The cell viability was measured using the Cell Counting Kit-8 assay.

3. Results and discussion

3.1. Preparation and characterization of PFBT@Rox Lip nanoparticles

Poly[(9,9-dioctylfluorenyl-2,7-diyl)-alt-(benzo[2,1,3]thiadiazol-4,7-diyl)] (PFBT) and Roxadustat were self-assembled into liposomal nanoparticles (PFBT@Rox Lip) *via* nanoprecipitation using cholesterol, lecithin and 1,2-distearoyl-sn-glycero-3-phosphoethanolamine-poly(ethylene glycol)-2000 as surfactants (Fig. 1A). PFBT@Rox Lip nanoparticles had a uniform and transparent appearance in aqueous solutions. Transmission electron microscopy (TEM) analysis demonstrated that PFBT@Rox Lip nanoparticles were round in shape and ~50 nm in diameter (Fig. 1B). The hydrodynamic diameter of a PFBT@Rox Lip nanoparticle was 56 nm, as measured using dynamic light scattering (Fig. 1C). PFBT@Rox Lip nanoparticles were dispersed in water, phosphate-buffered saline (PBS), and Dulbecco's modified Eagle medium. The stability examination of PFBT@Rox Lip nanoparticles suggested no obvious aggregation was observed in various aqueous solutions within 14 days, implying good stability for PFBT@Rox Lip nanoparticles (Fig. 1D and Supporting Information Fig. S1). The encapsulation rates of Roxadustat and PFBT were calculated to be 70 % and 95 % respectively from established standard curves by measuring absorbance values. The loading rates of Roxadustat and PFBT were determined to be 15% and 64% respectively (Supporting Information Fig. S2). We also investigated the Roxadustat release *in vitro* from PFBT@Rox Lip nanoparticles. The results showed that abundant PFBT and Roxadustat were released from PFBT@Rox Lip upon incubating PFBT@Rox Lip in PBS containing H_2O_2 (pH 7.4) (Supporting Information Fig. S3). A slower release of drug behavior was observed at the condition without irradiation, suggesting 39% and 19.8% of PFBT and Roxadustat release after 24 h incubation, respectively. However, upon light irradiation for 1h, a marked increase in the release of PFBT and Roxadustat was detected with a cumulative drug release of 98% and 48.8% for PFBT and Roxadustat, respectively after 24 h (Fig. S3). Next, the zeta potential of PFBT@Rox Lip nanoparticles was determined to be −12.3 mV, which is conducive to maintaining nanoparticle stability in the bloodstream (Fig. 1E). In addition, the ultraviolet−visible−near infrared absorption and emission spectra were analyzed and showed that PFBT@Rox Lip nanoparticles had an absorption peak at ~470 nm and an emission peak at ~540 nm (Fig. 1F). To gain a deeper understanding of the excitation properties of PFBT-conjugated polymers, we performed theoretical calculations to reveal the process of *in situ* self-assembling coating and photophysical properties of the obtained nanoparticles. As shown in Fig. 1G and H, the density functional theory calculations demonstrated that the PFBT $\Delta E_{S1\text{-}T1}$ value was 0.26 eV. Such a low $\Delta E_{S1\text{-}T1}$ value is beneficial for the energy transfer from S_1 to T_1 and generates a sensitized T_1 state, and it enables the energy transfer to the adjacent O_2 for $^1O_2$ generation efficiency. In addition, the energy gap between the highest occupied molecular orbital and the lowest unoccupied molecular

of type I/II ROS generation by PFBT@Rox Lip nanoparticles including energy levels and $\Delta E_{S1\text{-}T1}$ values of PFBT calculated using density functional theory (B3LYP/6-31G (d, p)). (I) DCFH fluorescence intensities of PFBT@Rox Lip nanoparticles at different time points after the irradiation with white light. (J) Electron spin resonance (ESR) spectra of the PFBT@Rox Lip nanoparticles with TEMP as $^1O_2$ trapper. (K) ESR spectra of the PFBT@Rox Lip nanoparticles with DMPO as $O_2^{-}\cdot$ trapper. (L) ESR spectra of the PFBT@Rox Lip nanoparticles with DMPO as ·OH trapper.

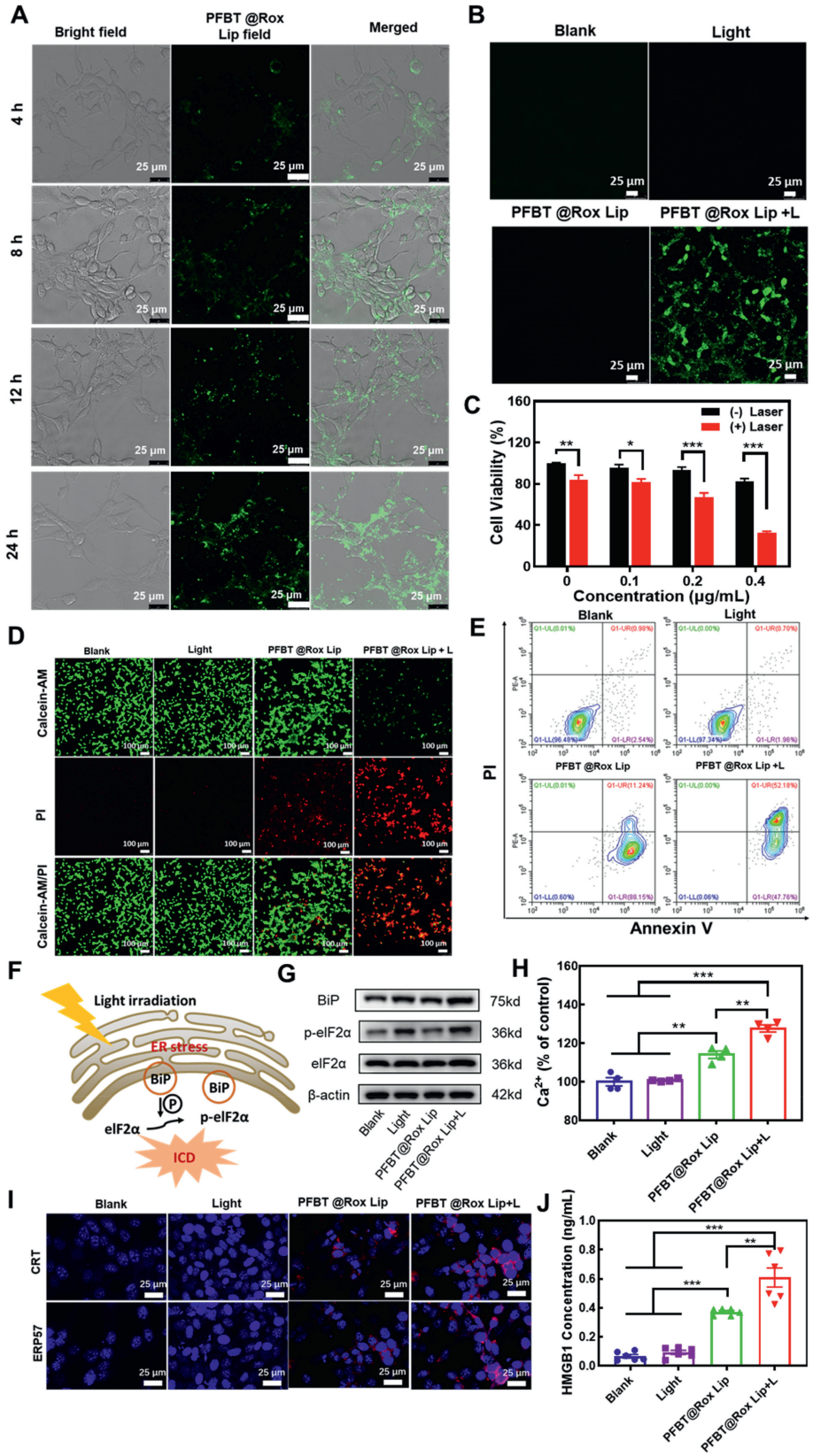


Figure 2 *In vitro* performance of PFBT@Rox Lip in cancer cells. (A) Internalization analysis of PFBT@Rox Lip nanoparticles by Colon-26 tumor cells at 4, 8, 12 and 24 h after the start of the treatment.scale bar = 25 μm. (B) Confocal laser scanning microscopy images of ROS using DCFH-DA staining. scale bar = 25 μm. (C) Cell viability of Colon26 tumor cells under the treatment of PFBT@Rox Lip nanoparticles with or without white light irradiation (n = 5). (D) Live/dead cell analysis using Calcein-AM (green)/PI (red) staining after different treatments of Colon26 cells. scale bar = 100 μm. (E) Detection of apoptosis of Colon-26 cells with Annexin V/PI staining using flow cytometry. (F) The

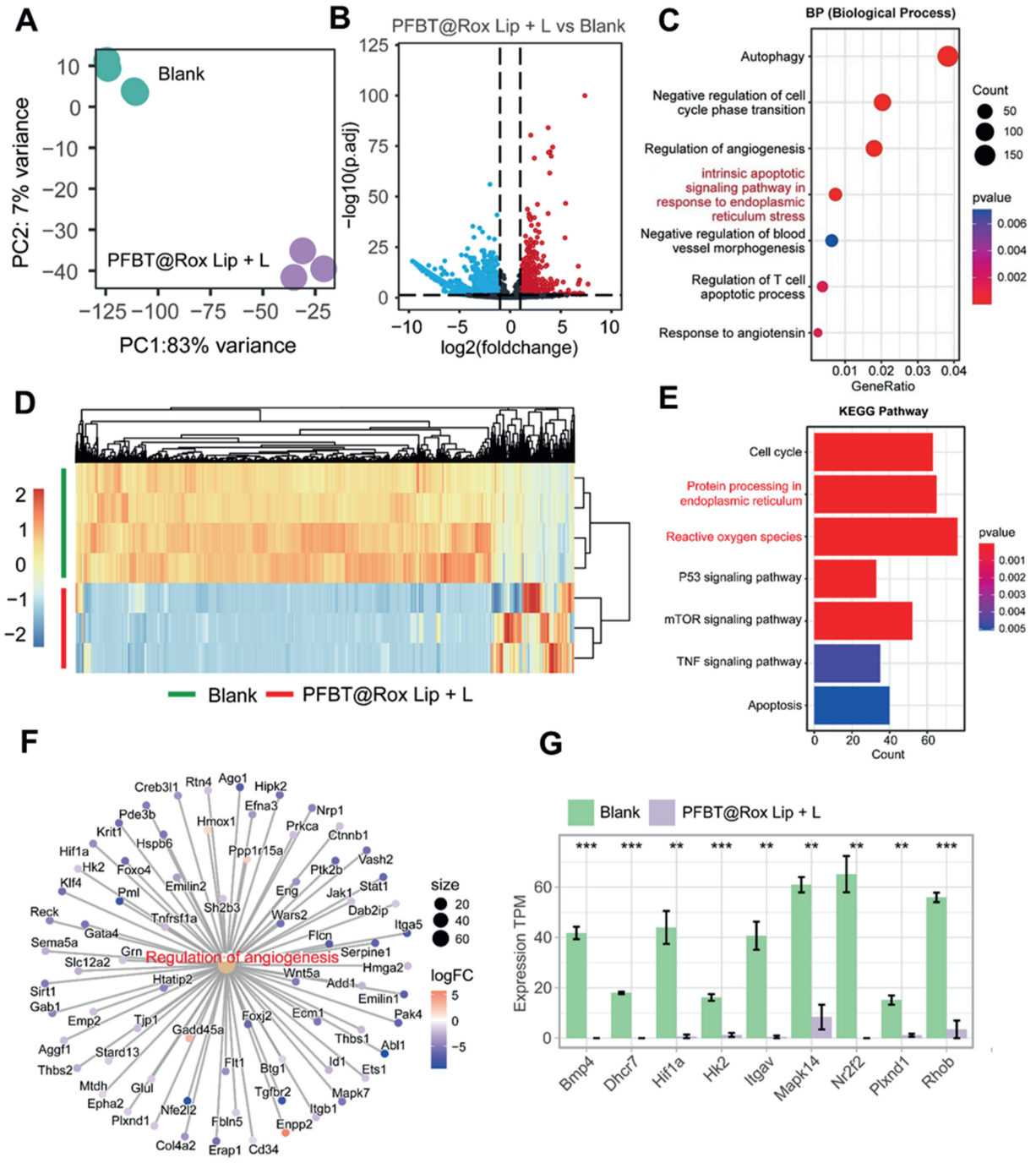


Figure 3 RNA sequencing (RNA-Seq) analysis of Colon26 cells treated with PFBT@Rox Lip + L. (A) Principal component analysis in blank and PFBT@Rox Lip + L groups in Colon26 cells. (B) Volcano plot indicating genes differentially expressed between the PFBT@Rox Lip + L and blank groups. Up-regulated and down-regulated genes in the treated group were illustrated using red and blue symbols, respectively. (C) Dot plot showing biological processes differentially regulated by the PFBT@Rox Lip + L treatment compared with those in the blank group according to the Gene Ontology enrichment analysis. (D) Heatmap showing the genes differentially expressed between the PFBT@Rox Lip + L and blank groups. (E) Bar plot showing the pathways differentially regulated in the PFBT@Rox Lip + L group compared with those in the blank group according to the KEGG pathway enrichment analysis. (F) Expression changes between PFBT@Rox Lip + L and Blank in the Angiogenesis GO term. (G) The expression of angiogenesis-related genes in PFBT@Rox Lip + L and Blank.

pathway of ER stress and ICD signaling activation. (G) Representative Western blot showing the expression levels of BiP, P-elF2α and elF2α in Conlon26 cells with various treatments. (H) Intracellular Ca^{2+} level and quantitative analysis after various treatments by flow cytometric analysis ($n = 3$). (I) Immunofluorescence staining of cell-surface CRT and ERp57 expression in various groups. scale bar = 25 μm. (J) Release of HMGB-1 from Colon26 cells after different treatments ($n = 5$). Data are presented as the mean ± SD. Statistical significance of treatment effects is illustrated as follows: $^{*}P < 0.05$, $^{**}P < 0.01$, and $^{***}P < 0.001$, ns, not significant.

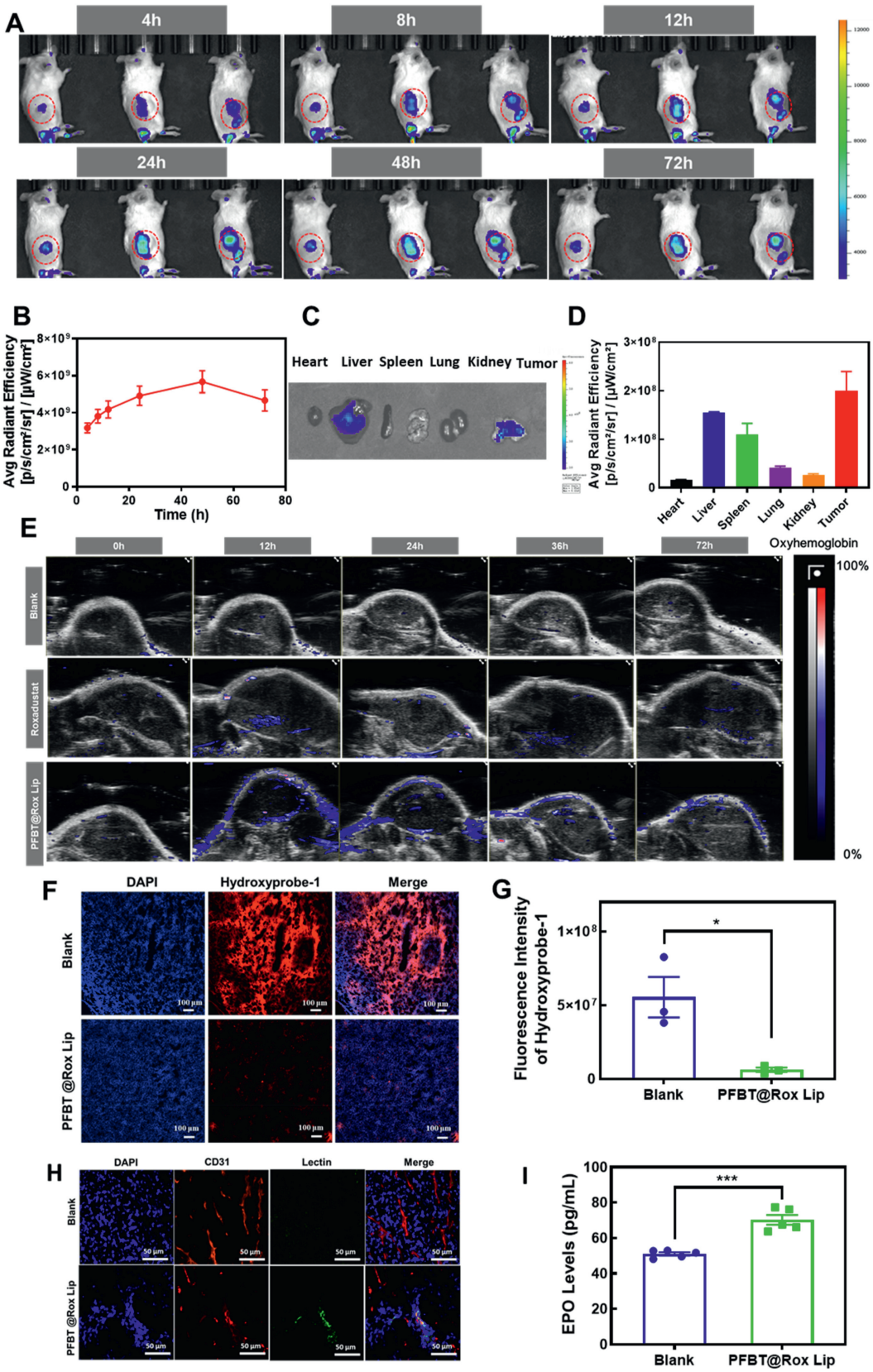


Figure 4 PFBT@Rox Lip nanoparticles exhibit good tumor targeting, restore tumor vessel function and reduce hypoxia. (A) *In vivo* imaging and (B) quantification of Cy5-labeled PFBT@Rox Lip nanoparticles in Colon26 tumors at different time points (4, 8, 12, 24, 48 and 72 h). (C) *Ex vivo* imaging and (D) quantification of Cy5-labeled PFBT@Rox Lip nanoparticles in major organs and dissected tumors ($n = 3$). (E) Photoacoustic imaging of Colon26 tumors showing O_2 levels at different time points (0, 12, 24, 36, 48 and 72 h) after the injection of PFBT@Rox

orbital (HOMO−LUMO) for the PFBT-conjugated polymer was calculated to be 3.2 eV. Full separation of the HOMO and LUMO is beneficial for the *in situ* self-assembling coating and promotes the generation of type II ROS. Because the PFBT-conjugated polymer possesses a π−electronic backbone structure, the excited PFBT* further transfers electrons to the surrounding O_2 or H_2O to produce superoxide radicals ($O_2\cdot^-$) and hydroxyl radicals ($\cdot$OH) (Supporting Information Fig. S4). In addition, PFBT energy levels measured using an ultraviolet photoelectron spectrometer showed an energy tendency similar to the calculated one for the conjugated polymer (Fig. 1G). Total ROS production by PFBT@Rox Lip nanoparticles was determined using the ROS probe 2,7-dichlorofluorescein diacetate (DCFH-DA). In the presence of ROS, DCFH-DA is oxidized to 2,7-dichlorofluorescin (DCF), which emits bright fluorescence at 525 nm. As shown in Fig. 1I, upon white light irradiation with a direct current for 6 min, the fluorescence intensity of DCF increased over time. However, there was no significant change in the fluorescence of DCFH without PFBT@Rox Lip nanoparticles, indicating that the latter sensitized the surrounding oxygen or water molecules to produce ROS. The identities of ROS ($^1O_2$, $\cdot$OH and $O_2\cdot^-$) were experimentally evaluated using electron paramagnetic resonance. Established methods typically use 2,2,6,6-tetramethylpiperidine (TEMP) as a probe for $^1O_2$, and 5,5-dimethyl-1-pyrroline-*N*-oxide (DMPO) as a spin-trap to detect $O_2\cdot^-$ and $\cdot$OH. The hyperfine splitting constants (aN, aH) and g factor for the spin adducts were used to examine the presence of each ROS. As shown in Fig. 1J, triplet peaks corresponding to typical TEMPO• signals were observed for white light irradiation (aN = 16.5 G, g = 2.0058), suggesting the appearance of $^1O_2$, in sharp contrast to the silent spectra for the untreated sample. The signals of the DMPO/$O_2^{\bullet-}$ adduct were also observed under the experimental conditions (Fig. 1K). In addition, as shown in Fig. 1L, •OH formation was also evidenced by the electron paramagnetic resonance signals of the DMPO/$\cdot$OH adduct (aN = aH = 14.8 G, g = 2.0031). Additionally, the frequently used photosensitizer Hematoporphyrin monomethyl ether (HMME), was also employed as a control to compare its capability of ROS generation with that of PFBT. We found that PFBT showed a more efficient capability of ROS generation when compared with HMME, indicating that PFBT is an excellent photosensitizer. (Supporting Information Fig. S5). Together, these results indicated that PFBT@Rox Lip nanoparticles showed excellent Type I and Type II ROS generation capacities.

3.2. In vitro therapeutic effect of PFBT@Rox Lip nanoparticles and underlying mechanisms

Given the capacity of abundant ROS generation by PFBT@Rox Lip nanoparticles, we next evaluated *in vitro* anti-tumor efficacy of PDT in the Colon26 cell line. The therapeutic efficacy of a nanomedicine is highly dependent on its cellular uptake. The uptake of PFBT@Rox Lip nanoparticles by Colon26 cells was observed using confocal laser scanning microscopy. As shown in Fig. 2A, the intracellular green fluorescence gradually became stronger with the extension of the incubation time from 4 to 24 h, indicating that PFBT@Rox Lip nanoparticles could be internalized into cells, which would facilitate the induction of the photodynamic effect. ROS can induce cell death. To verify the *in vitro* anti-tumor efficacy of the PFBT@Rox Lip nanosystem that would be achieved by releasing ROS, *in vitro* ROS production was detected using a DCFH-DA probe, and the cell viability in different treatment groups was examined using the Cell Counting Kit-8 assay. As shown in Fig. 2B and C, PFBT@Rox Lip nanoparticles produced a large amount of ROS after light irradiation, and the cytotoxicity of the combination treatment showed the inhibition of cell viability to the greatest extent. However, Roxadustat and PFBT alone just slightly induced viability suppression compared with PFBT@Rox Lip (Supporting Information Fig. S6). In addition, we also evaluated the PDT effects of PFBT and PFBT@Rox Lip under hypoxic conditions (2%). PFBT@Rox Lip plus irradiation could still significantly repress cancer cell viability (Supporting Information Fig. S7). Subsequently, calcein-AM/propidium iodide staining was performed to observe cell survival. As shown in Fig. 2D, PFBT@Rox Lip-treated cells showed red fluorescence, which was not observed in "blank" and "light alone" groups, indicating that PFBT@Rox Lip nanoparticles alone could induce cancer cell death, possibly resulting from a small quantity of toxicity itself. However, treatment with a combination of PFBT@Rox Lip nanoparticles and light led to the most conspicuous red fluorescence and weak green fluorescence in the cells when compared with other control groups, which further demonstrated that PFBT@Rox Lip nanoparticles can trigger ROS production under white light, eventually killing cancer cells. This observation aligns with the results of the Cell Counting Kit-8 assay. Additionally, cell cycle analysis with the annexin-V/propidium iodide staining showed that the proportion of early apoptotic cells (annexin-V^+) in the PFBT@Rox Lip alone group was significantly higher than that in the control group, consistent with the results of calcein-AM/propidium iodide assay, and notably, the proportion of late apoptotic cells (annexin-V^+/PI^+) in the PFBT@Rox Lip nanoparticles + light (PFBT@Rox Lip + L) group was 41% higher than the apoptotic fraction of cells treated with PFBT@Rox Lip alone and another two control groups (Fig. 2E). This finding further confirmed that PDT had a prominent *in vitro* killing effect on cancer cells. At the same time, we also examined the cytotoxic effect of PFBT@Rox Lip on NCM460, a normal intestinal epithelial cell with varying concentrations. PFBT@Rox Lip nanoparticles alone did not produce significant viability inhibition to normal intestinal epithelial cells, indicating good safety (Supporting Information Fig. S8). Taken together, these results demonstrate that the PFBT@Rox Lip system potently decreased the viability of cancer cells through ROS generation under irradiation with white light. Given that excessive ROS generation causes the ER stress, we further examined the expression of ER stress-related proteins, such as BiP and phosphorylated elF2α. Our data suggested that BiP and phosphorylated elF2α levels were increased after the combined treatment with PFBT@Rox Lip nanoparticles and light, indicating that PDT caused severe ER stress (Fig. 2F and G). Excess ROS also causes

Lip nanoparticles or Roxadustat. (F) Hypoxia evaluation using immunofluorescent staining after the treatment with hypoxyprobe-1. scale bar = 100 μm. (G) Quantitative analysis of the hypoxia level after the treatment with hypoxyprobe-1 (n = 3). (H) Vascular normalization evaluation using immunofluorescent staining. scale bar = 50 μm. (I) The EPO levels after the treatment with PFBT@Rox Lip. Data are presented as the mean ± SD. Statistical significance of treatment effects is illustrated as follows: *P < 0.05, **P < 0.01, and ***P < 0.001, ns, not significant.

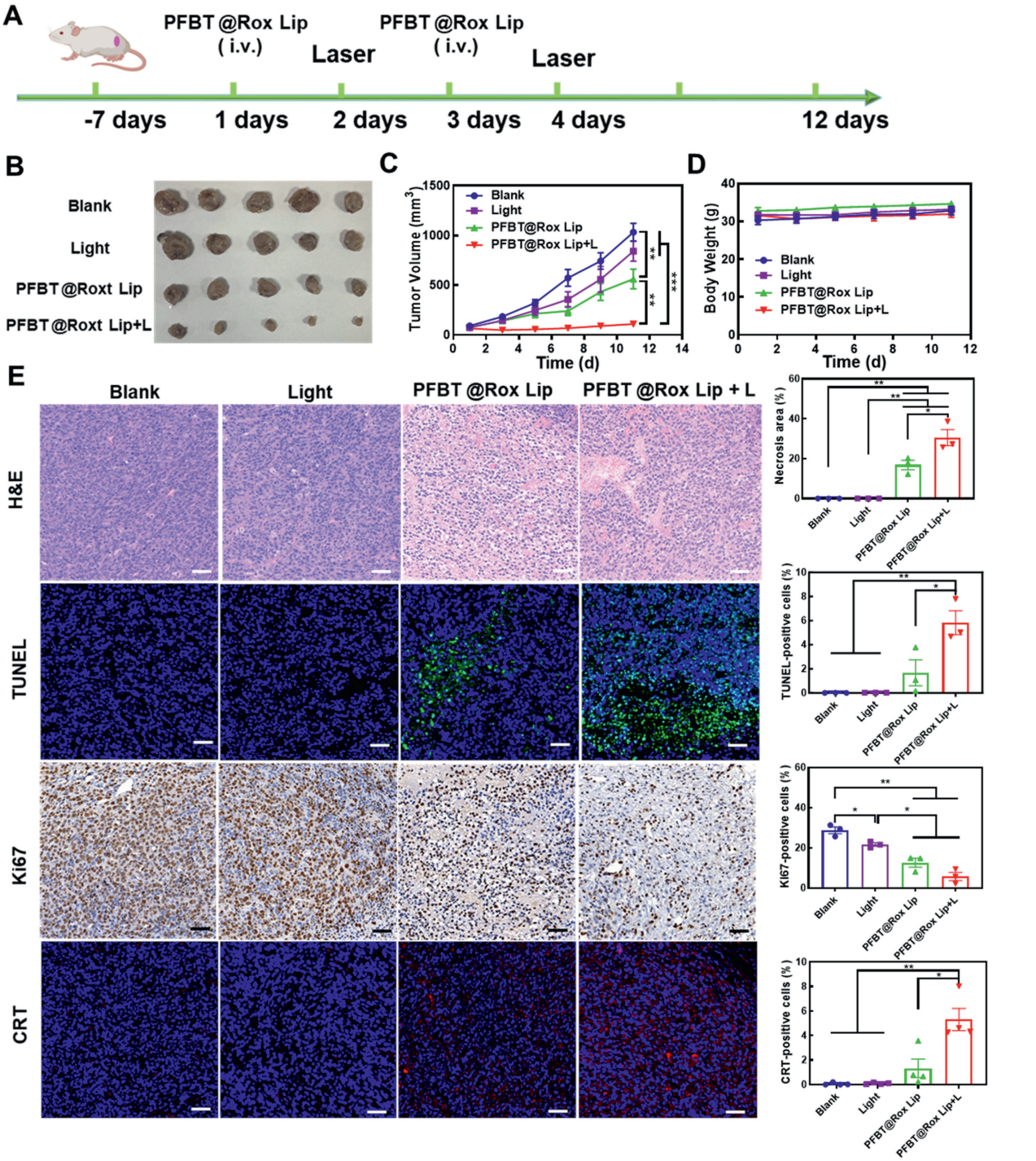


Figure 5 Assessment of therapeutic efficiency of PFBT@Rox Lip + L. (A) Schematic illustration of the *in vivo* therapeutic schedule. (B) Tumor images at the end of the treatment ($n = 5$). (C) Tumor growth curves in the four treatment groups during the 11 days ($n = 5$). (D) Body weight of the mice in different treatment groups during the experiment ($n = 5$). (E) Representative images and qualification of the H&E, TUNEL, Ki67, and CRT staining in the tumor tissues ($n = 3$). scale bar = 50 μm. Data are presented as the mean ± SD. Statistical significance of treatment effects is illustrated as follows: $^{*}P < 0.05$, $^{**}P < 0.01$, and $^{***}P < 0.001$, ns, not significant.

severe oxidative stress in the mitochondria and disrupts calcium homeostasis, eventually leading to the release of calcium from the mitochondria into the cytoplasm *via* the mitochondrial transition pores. As shown in Fig. 2H and Supporting Information Fig. S9, intracellular calcium levels were higher in the Colon26 cells incubated with PFBT@Rox Lip nanoparticles under white light than in the cells receiving control treatments. Interfering with intra/extracellular ion homeostasis not only induces tumor cell death but also ICD in tumor cells. Additionally, the ICD effect triggered by PDT in tumor cells was assessed by the translocation of CRT, ERp57 and the release of HMGB1. Immunofluorescence images indicated that PFBT@Rox Lip plus light irradiation

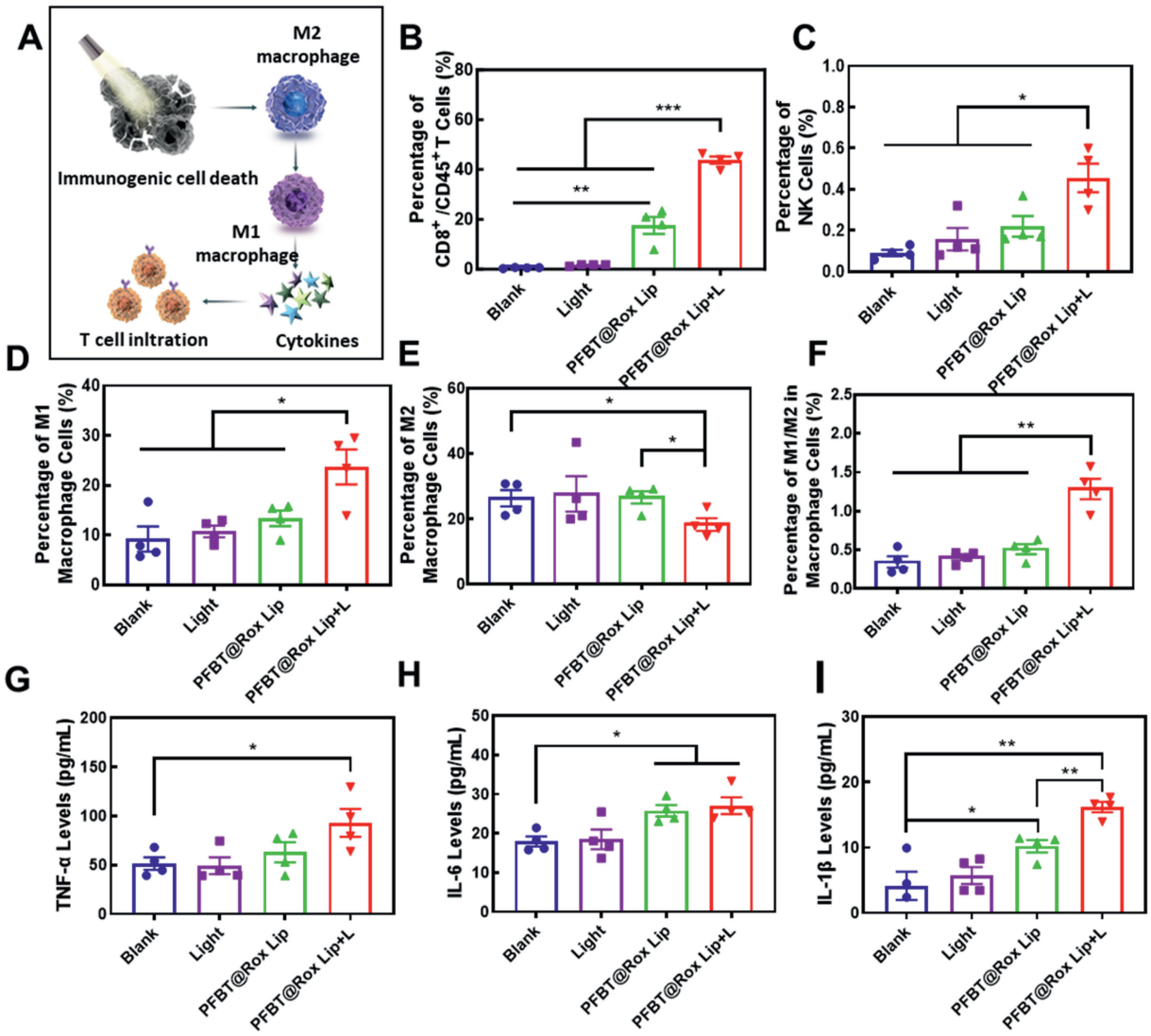


Figure 6 PFBT@Rox Lip nanoparticles plus irradiation remodels TME on tumor-bearing mice. (A) Schematic illustration for the effect of PDT treatment on the immunosuppressive tumor microenvironment. (B) The proportions of $CD8^+$ T cell ($CD3^+CD8^+$) populations within tumors. (C) The proportions of NK cell populations within tumors. (D) Proportions of M1 macrophages and (E) M2 macrophages in tumor tissues from mice after various treatments, were analyzed by flow cytometry. (F) The M1/M2 macrophage ratio in mice with Colon26 tumors after various treatments ($n = 4$). (G) The levels of secreted TNF-α, (H) IL-6, and (I) IL-1β in Colon26 tumors at the end of the treatment ($n = 4$). Data are presented as the mean ± SD. Statistical significance of treatment effects is illustrated as follows: $^*P < 0.05$, $^{**}P < 0.01$, and $^{***}P < 0.001$, ns, not significant.

induced obvious translocation of CRT and ERp57 compared with other groups. Moreover, the release of HMGB1 from Colon26 cancer cells was also increased correspondingly. These results demonstrate that PFBT@Rox Lip plus light irradiation could initiate ICD in cancer cells, thereby potentially provoking anti-tumor immunity (Fig. 2I and J). In addition, given that Roxadustat is an EPO inducer which could possibly alleviate hypoxia, we detected the expression of EPO protein after treatment with PFBT@Rox Lip plus light irradiation. The data clearly showed that EPO levels were increased more after the combined treatment with PFBT@Rox Lip nanoparticles plus light compared with nanoparticles alone and PBS, indicating that light irradiation could accelerate the release of Roxadustat from PFBT@Rox Lip nanoparticles, and the nanoparticles could potentially re-oxygenate the tumor tissues after the release of Roxadustat upon irradiation (Supporting Information Fig. S10). Collectively, these results demonstrated that PFBT@Rox Lip nanoparticles could trigger ICD and increase EPO, potentially initiating strong anti-tumor responses and reshaping the TME *in vivo*.

3.3. RNA sequencing and analysis after the treatment of PFBT@Rox Lip nanoparticles pus light

To further explore the molecular mechanism of PDT in-depth, RNA-seq was used to explore the related pathways involved in the therapeutic effect of combined treatment with PFBT@Rox Lip nanoparticles and light in Colon26 cells. The principal component analysis showed a significant difference between the treatment and blank control groups, indicating an extensive change in the gene expression pattern after the PFBT@Rox Lip + L treatment

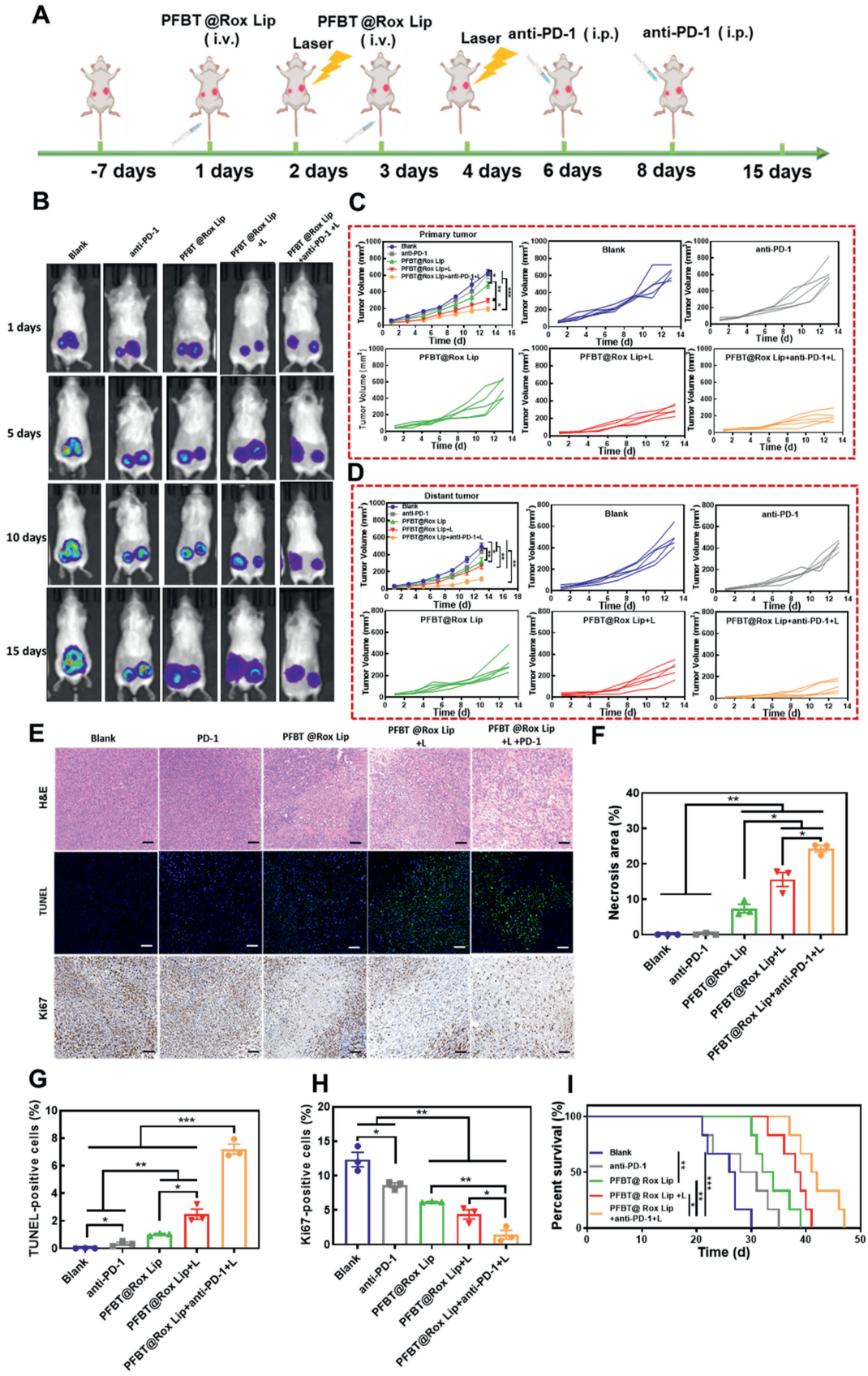


Figure 7 *In vivo* anti-primary and metastatic tumor efficacy with PFBT@Rox Lip-mediated PDT combined with PD-1 antibody. (A) Schematic diagram of the PFBT@Rox Lip PDT treatment combined with an antiPD-1 antibody. (B) *In vivo* imaging of the luciferase-expressing tumors on Days 1, 5, 10, and 15 in various treatment groups. (C) Primary and (D) distant (metastatic) tumor growth curves for each group and individual

(Fig. 3A). Further analysis showed 4172 differentially expressed genes (fold change $\geq$2, adjusted $P < 0.05$) after the PFBT@Rox + L treatment (Fig. 3B−E), among which 676 were up-regulated and 3496 were down-regulated (Fig. 3D). Enrichment analysis revealed that several pathways were enriched after the PFBT@Rox Lip + L treatment, such as those related to ER stress-induced apoptosis, ROS production, angiogenesis, and cell cycle (Fig. 3C and E). Notably, almost all genes involved in angiogenesis were down-regulated (Fig. 3F and G). These results suggested that PFBT@Rox Lip nanoparticles under light irradiation could inhibit cancer cells through a complex network probably initiated by ROS production *via* photodynamic activity.

3.4. PFBT@Rox Lip could accumulate into tumor targeting, normalize tumor blood vessels, and improve hypoxia in Colon26 tumor-bearing mice

The efficient accumulation of nanoparticles into tumor tissues is a key factor in realizing therapeutic examination. We subsequently assessed the tumor-targeting ability of PFBT@Rox Lip nanoparticles. Cy5-labeled PFBT@Rox Lip nanoparticles were injected into Colon26 tumor-bearing mice to determine their distribution and tumor-specific enrichment at different time points. As shown in Fig. 4A and B, and Supporting Information Fig. S11, the fluorescence signals for Cy5-PFBT@Rox Lip detected by an *in vivo* imaging system were mainly localized at the tumor sites 4 h after administration. Cy5-PFBT@Rox Lip could be highly enriched in the tumors after systemic administration in the Colon26 tumor-bearing mice; whereas free Cy5 did not show a good ability for tumor imaging (Fig. S11). The fluorescence signals increased gradually over time and peaked at 48 h after injection, and apparent fluorescence signals were still detectable at the tumor site even at 72 h. These results demonstrated that PFBT@Rox Lip nanoparticles could efficiently target tumors and retain in tumor tissues for at least 72 h, thereby providing a sufficient time window for PDT application. For detailed tissue distribution of PFBT@Rox Lip nanoparticles, ex *vivo* fluorescence images of isolated organs collected 72 h post-injection disclosed the strongest fluorescence signals associated with Cy5-labeled PFBT@Rox Lip nanoparticles at the tumor site (Fig. 4C and D). This might be because the Colon26 tumors are highly vascularized, facilitating the passive targeting of liposomes to tumor sites. This finding was consistent with the *in vivo* imaging results, which further confirmed the nanosystem's precise targeting and accumulation properties. Hypoxia, caused by abnormal tumor vasculature and rapid tumor growth, is the main feature of solid tumors and plays an important role in their development and occurrence. Given our observation that Roxadustat in PFBT@Rox Lip nanoparticles could increase EPO levels which potentially elevated the oxygen delivered by increased hemoglobin, we thus examined whether our nanosystem could at least partially decrease the degree of hypoxia in the Colon26 tumor model *in vivo*. Firstly, we measured EPO levels in solid tumors after two doses of nanoparticle administration, the data showed that PFBT@Rox Lip nanoparticles indeed increased EPO levels. The oxygenation of tumor tissues treated with PFBT@Rox Lip nanoparticles was further analyzed by photoacoustic imaging. According to the different absorbance values by oxygenated hemoglobin (λ = 850 nm) and deoxyhemoglobin (λ = 750 nm), the oxygenated hemoglobin levels at different time points after intravenous injection (i.v.) were recorded by photoacoustic imaging, accompanied with B-mode ultrasound imaging based on the saturated O_2 levels. As shown in Fig. 4E, the saturated O_2 levels gradually increased over time in tumors treated with nanoparticles or Roxadustat. However, it seemed that nanoparticles containing Roxadustat could result in better oxygenation in tumors, indicating that the nanosystem enhances the delivery of Roxadustat and induces stronger oxygenation in tumor tissues. Nevertheless, the saturated O_2 levels gradually decreased after 24 h injection for both nanoparticles or Roxadustat (Fig. 4E). This might be due to the fact that Roxadustat generally reaches its functional peak effect 8−24 h after administration[33]. The extent of hypoxia in tumors treated was determined with pimonidazole hydrochloride (hypoxyprobe-1) after treatment with PFBT@Rox Lip nanoparticles; The staining indicated that the untreated control tumors showed strong hypoxia signals, whereas the hypoxia level was significantly reduced in the tumors treated with PFBT@Rox Lip nanoparticles (Fig. 4F and G), suggesting that the latter relieves hypoxia in solid tumors and reoxygenates the hypoxic tumor microenvironment. It has been demonstrated that tumor hypoxia results in abnormal angiogenesis and aberrant vascular structure, which accelerate the tumor development in turn. We wondered whether PFBT@Rox Lip nanoparticles could normalize tumor blood vessels and improve vessel perfusion due to hypoxia alleviation. Subsequently, we assessed tumor vascular perfusion with the staining of vessel marker CD31 (red) for endothelial cells and pre-injected FITC-lectin (green) for perfusion. Compared with the blank group, the PFBT@Rox Lip group displayed better vessel perfusion, which indicated that PFBT@Rox Lip nanoparticles could improve vascular functionality and normalize the tumor blood vessels. These results together demonstrated that PFBT@Rox Lip could efficiently target tumors and normalized tumor vessels by relieving hypoxia *via* Roxadustat (Fig. 4H and I). The improvement in oxygenation and alleviation of hypoxia strongly indicated that the use of PFBT@Rox Lip nanoparticle showed the greatest promise for *in vivo* cancer therapy.

3.5. PDT mediated by PFBT@Rox Lip plus irradiation executed prominent in vivo anti-tumor activity

Having demonstrated *in vivo* tumor targeting ability and hypoxia alleviation, we further investigated the half-life of PFBT@Rox Lip nanoparticles after intravenous administration and *in vivo* anti-tumor effect of the nanosystem in Colon26 tumor-bearing mice. First, the half-life of PFBT@Rox Lip nanoparticles was estimated to be approximately 1.8 h after intravenous administration by examining the intrinsic fluorescence intensity of PFBT@Rox Lip nanoparticles at different time points (Supporting Information Fig. S12). Next, *in vivo* anti-tumor performance was further explored. The therapeutic schedule for the *in vivo* assessment was illustrated in Fig. 5A. Mice were randomly divided into four groups: 1) blank (PBS), 2) light alone, 3) PFBT@Rox Lip

mice during the treatment period (n = 5). (E) Images of distant (metastatic) tumor sections with H&E, TUNEL, and Ki67 staining. (F) Quantification of H&E, (G) TUNEL, and (H) Ki67 staining (n = 3). (I) Survival curves of mice based on primary tumors in different treatments during the treatment period (n = 6). Data are presented as the mean ± SD. Statistical significance of treatment effects is illustrated as follows: *$P < 0.05$, **$P < 0.01$, and ***$P < 0.001$, *n*s, not significant.

alone, and 4) PFBT@Rox Lip + L. The PFBT@Rox Lip solution (150 μL, 50 μg/mL) and PBS were administered intravenously to mice on the 1st and 3rd day of the experiment, respectively, when the tumor volume reached about 100 mm^3. In 24 h after the solution administration, mice from the light alone and PFBT@Rox Lip + L groups were given 40 mW/cm^2 white light irradiation for 30 min. Body weight and tumor volume were monitored every 2 days, and the mice were sacrificed on the 12th day. The data indicated that the largest tumor growth inhibition was attained in animals that received the treatment with the PFBT@Rox Lip + L group (Fig. 5B and C, and Supporting Information Fig. S13). This efficacy was likely attributed to the potent suppression of tumor cell viability caused by ROS production, apoptosis, ICD and potential anti-tumor immunity induced by relieving the hypoxia under PDT with PFBT@Rox Lip nanoparticles. No significant influence on body weight, blood parameters and tissue morphology was observed in any group (Fig. 5D, Supporting Information Figs. S15−S17), which implicated the excellent bio-safety of the therapeutic modality. Subsequently, tumor sections from each group were stained with hematoxylin and eosin (H&E), terminal deoxynucleotidyl transferase dUTP nick end labeling (TUNEL), and antibody against the proliferation marker Ki-67 to assess the effects of combined treatments with PFBT@Rox Lip nanoparticles and irradiation on tumor necrosis, apoptosis, and proliferation. As shown in Fig. 5E, no evident cell death was observed in the two control groups, whereas more apoptotic cells and fewer proliferating cells were observed in the PFBT@Rox Lip group, indicating that PFBT@Rox Lip nanoparticles alone could produce an anti-tumor effect to some extent, consistent with *in vitro* data shown before. Of note, tumor tissues from mice receiving the PFBT@Rox Lip + L treatment showed the highest percentage of tumor cell apoptosis and the lowest proportion of cell proliferation, confirming the strong anti-tumor effect of the combined treatment, highly consistent with the tumor volume data. Considering that the exposure of the CRT protein on the cell surface following PDT is a crucial event for ICD, CRT immunofluorescence staining in tumor tissues was also performed. Minimal cell-surface CRT exposure (red) was observed in the two control groups and the PFBT@Rox Lip group, whereas the PFBT@Rox Lip + L indicated a higher extent of CRT exposure. This was in accordance with the *in vitro* results, confirming the induction of ICD by PDT and providing a plausible explanation for the potent tumor inhibition by combination therapy. To exclude the possible influence of Roxadustat and PFBT alone on tumor progression, we also determined the tumor development in tumor-bearing mice treated with Roxadustat and PFBT alone as illustrated in Fig. S14A. Both of them alone did not affect the tumor growth (Fig. S14B). Meanwhile, Roxadustat and PFBT alone did not reshape the tumor microenvironment based on the analysis for infiltrated T cells and macrophage polarization after treatment (Figs. S14C−S14E). Collectively, these results further demonstrate that PDT mediated by PFBT@Rox Lip plus irradiation possesses excellent biocompatibility and exhibits outstanding anti-tumor performance in tumor-bearing mice.

3.6. PFBT@Rox Lip nanoparticles plus irradiation reshaped TME

PDT has been reported to stimulate T-cell infiltration by triggering an ICD effect which enhances antigen presentation of APCs (antigen-presenting cells). Next, we explored how PDT affects the microenvironment of Colon26 subcutaneous tumors by analyzing immune cells and cytokines (Fig. 6A). We found that $CD8^+$ T cell infiltration was significantly increased in the PFBT@Rox Lip + L group (40%) compared to control groups, indicating that PDT promotes greater immune responses *in vivo* possibly owing to ICD induction and vessel normalization (Fig. 6B and Supporting Information Fig. S18). The percentage of NK cells in animals receiving the combination treatment (0.45%) was significantly elevated when compared with the Light alone (0.15%) and PFBT@Rox Lip alone (0.22%), which implies that PFBT@Rox Lip nanoparticles significantly promote the recruitment of NK cells under light irradiation (Fig. 6C). About the effect on macrophage polarization, the highest proportion of the M1 macrophages (27%) and the lowest proportion of the M2 macrophages (18%) among all treatment groups were observed in the PFBT@Rox Lip + L group (Fig. 6D−F, and Supporting Information Fig. S19), suggesting that PDT promotes macrophage transition from M2 phenotype towards the M1 phenotype. It has been demonstrated that photodynamic immunotherapy not only directly kills cancer cells but also reprograms TME[34-36]. Typically, photosensitizers for PDT can efficiently produce ROS in tumors under localized light irradiation, which induces immunogenic cell death (ICD) besides apoptosis in cancer cells. The dying tumor cells release tumor-associated antigens (TAAs) and immunogenic damage-related molecular patterns (DAMPs) such as ecto-CRT/ERp57, HMGB1 et al., which could interact with tumor-associated macrophage (TAMs), induce more M1 polarization and enhance phagocytosis of macrophages to dying cancer cells, ultimately increasing the infiltration of T cells[37,38]. Next, serum levels of cytokines critically important for the immune regulation (TNF-α, IL-1β, and IL-6) were analyzed using ELISA. As shown in Fig. 6G−I, TNF-α, IL-1β, and IL-6 levels in the PFBT@Rox Lip + L group were significantly up-regulated than those in other control groups, further confirming a powerful immune response triggered by PDT *in vivo*. Overall, these results supported the notion that PFBT@Rox Lip-mediated photoimmunotherapy efficiently increased the infiltration of $CD8^+$ T cells, and NK cells, induced the M1 polarization of macrophages and up-regulated inflammatory cytokine secretion. This novel PDT modality not only affords excellent anti-tumor performance but also reprograms the TME and induces anti-tumor immunity.

3.7. PFBT@Rox Lip-mediated PDT potentiated the anti-tumor efficacy of PD-1 antibody and exerted anti-primary and metastatic tumor effects

Considering that PDT induces a powerful immune response, especially more $CD8^+$ T cell infiltration, the PFBT@Rox Lip + L treatment combined with checkpoint blockades, such as anti-PD-1 antibody, which is currently one of the preferred immunotherapy regimens, might further amplify anti-tumor efficacy and potentially suppress metastasis and tumor recurrence. A commonly used 4T1-luc cell line was implanted bilaterally into BALB/c mice to simulate primary and metastatic tumors. When the primary tumor volume reached 100 mm^3, the mice were randomly divided into five groups: 1) blank (PBS), 2) anti-PD-1 antibody alone, 3) PFBT@Rox Lip, 4) PFBT@Rox Lip + L, and 5) PFBT@Rox Lip + L + anti-PD-1 antibody. According to the therapeutic schedule shown in Fig. 7A, PFBT@Rox Lip nanoparticle suspension (150 μL, 50 μg/mL) and PBS solution were administered intravenously on the 1st and 3rd day, respectively. Animals in the light-exposed groups received irradiation with 40 mW/cm^2 white light for 30 min on the 2nd and 4th day. Meanwhile, mice in both

the anti-PD-1 antibody alone and PFBT@Rox Lip + L + anti-PD-1 antibody groups were intraperitoneally administered an anti-PD-1 antibody (10 mg/kg) on Days 6 and 8. Body weight and bilateral tumor volumes of the mice were measured every 2 days during the treatment period. Tumor images were obtained using an *in vivo* imaging system on Days 1, 5, 10, and 15. As shown in Fig. 7B−D, imaging and direct bilateral tumor volume consistently showed that primary tumors treated with PBS, PD-1 antibody alone, or PFBT@Rox Lip nanoparticles grew rapidly, reaching almost 600 mm^3 on the 13th day. This was consistent with the data observed in the Colon26 subcutaneous tumor model. However, the combined treatment with PFBT@Rox Lip + L + anti-PD-1 antibody effectively repressed the growth of primary tumors. For untreated contralateral tumors, the anti-PD-1 treatment alone was minimally effective against distant tumors, possibly because of the high malignancy of 4T1 tumors which are refractory and less responsive to PD-1 therapy. As expected, distant tumor growth was remarkably suppressed in the PFBT@Rox Lip + L + anti-PD-1 combination group, suggesting that the triple combination treatment induced strong systemic anti-tumor immunity *in vivo*. Finally, H&E, TUNEL, and Ki-67 staining performed on distal tumor sections showed that the triple combination treatment indicated the strongest tumor necrosis and apoptosis as well as less tumor cell proliferation when compared with other treatment groups (Fig. 7E−H). Moreover, mice treated with PFBT@Rox Lip + L + anti-PD-1 antibody showed the longest survival time among all groups (Fig. 7I), indicating the advantages of the combination therapy in survival extension. Together, these results revealed that PFBT@Rox Lip + L combined with ICB immunotherapy could achieve the best anti-tumor efficacy, suggesting the great potential of the immunosynergistic activity of PDT for cancer treatment and greatly warranting potential translation in clinical settings in the future.

4. Conclusions

In this study, we designed and synthesized a multifunctional nanosystem composed of a conjugated polymer (PFBT) and an EPO induce (Roxadustat), realizing tumor photodynamic therapy with ROS production *via* both of the type I/II reactions. This nanosystem could effectively alleviate tumor hypoxia and promote vascular normalization in the tumor microenvironment. Upon irradiation with white light, ROS generated by PFBT@Rox Lip nanoparticles induced ER stress and resulted in the release of DAMPs which efficiently initiated ICD. Moreover, PFBT@Rox Lip nanoparticles reshaped TME, indicative of M1 polarization of tumor-associated macrophages, the recruitment of NK cells and $CD8^+$ T cells, and the up-regulated secretion of inflammatory factors. PFBT@Rox Lip-mediated PDT combined with an anti-PD-1 antibody could further maximize the anti-tumor efficacy, which strongly inhibited primary tumor growth and metastasis. Overall, our findings indicate that this novel nanosystem offers a promising PDT strategy for potential clinical applications and is a great candidate for combination therapy with immunotherapy.

Acknowledgments

This work was supported by National Key Research and Development Program of China (No. 2022YFC2303600, 2020YFA0908000), Scientific and technological innovation project of China Academy of Chinese Medical Sciences (No. CI2023D003, CI2023D008, CI2021B014), the Innovation Team and Talents Cultivation Program of National Administration of Traditional Chinese Medicine (No. ZYYCXTD-C-202002, China), the CACMS Innovation Fund (No. CI2023E002, CI2021A05101 and CI2021A05104, China), the Science and Technology Foundation of Shenzhen (No. JCYJ20210324115800001, JCYJ20210324113608023, China), the Science and Technology Foundation of Shenzhen (Shenzhen Clinical Medical Research Center for Geriatric Diseases); the Shenzhen Medical Research Fund (No. B2302051, China), Shenzhen Governmental Sustainable Development Fund (No. KCXFZ20201221173612034, China), Shenzhen Fund for Guangdong Provincial High-level Clinical Key Specialties (No. SZGSP001, China), the Distinguished Expert Project of Sichuan Province Tianfu Scholar (No. CW202002, China), the Shenzhen Science and Technology Innovation Commission (No. JCYJ20200109120205924, JCYJ20210324114202008, China), GuangDong Basic and Applied Basic Research Foundation (No. 2021A1515012164, 2022A1515110745, China), International Science and Technology Cooperation for Shenzhen Technology Innovation Plan (No. GJHZ20200731095411034, China). Chinese Postdoctoral Science Foundation (No. 2022M712190, China) and Guang Dong Basic and Applied Basic Research Foundation (No. 2022A1515110745, China). The Key Special Project of "Strategic Science and Technology Innovation Cooperation" from the National Key R&D Program of China (No. 2023YFE0204500, China), the Shenzhen Science and Technology Innovation Committee (SZSTI) (No. RCYX20221008092950121, China), the National Natural Science Foundation of China (No. 82373775, 82070517).

Author contributions

Haitao Yuan: Writing − original draft, Formal analysis, Conceptualization. Xiaoxian Wang: Formal analysis, Data curation. Xin Sun: Formal analysis, Data curation. Di Gu: Formal analysis. Jinan Guo: Formal analysis. Wei Huang: Formal analysis, Data curation. Jingbo Ma: Formal analysis, Data curation. Chunjin Fu: Formal analysis, Data curation. Da Yin: Formal analysis, Data curation. Guohua Zeng: Supervision. Ying Long: Supervision, Funding acquisition. Jigang Wang: Supervision, Resources, Funding acquisition. Zhijie Li: Supervision, Funding acquisition.

Conflicts of interest

The authors have no conflicts of interest to declare.

Appendix A. Supporting information

Supporting information to this article can be found online at https://doi.org/10.1016/j.apsb.2025.04.007.

References

1. Zhang Y, Kurupati R, Liu L, Zhou XY, Zhang G, Hudaihed A, et al. Enhancing $CD8^+$ T cell fatty acid catabolism within a metabolically challenging tumor microenvironment increases the efficacy of melanoma immunotherapy. *Cancer Cell* 2017;**32**:377−91.e9.
2. Yuan WC, Lee YR, Huang SF, Lin YM, Chen TY, Chung HC, et al. A Cullin3-KLHL20 Ubiquitin ligase-dependent pathway targets PML to potentiate HIF-1 signaling and prostate cancer progression. *Cancer Cell* 2011;**20**:214−28.

3. Shi L, Zhang P, Liu X, Li Y, Wu W, Gao X, et al. An activity-based photosensitizer to reverse hypoxia and oxidative resistance for tumor photodynamic eradication. *Adv Mater* 2022;**34**:2206659.
4. Huang J, Zhuang C, Chen J, Chen X, Li X, Zhang T, et al. Targeted drug/gene/photodynamic therapy *via* a stimuli-responsive dendritic-polymer-based nanococktail for treatment of EGFR-TKI-resistant non-small-cell lung cancer. *Adv Mater* 2022;**34**:2201516.
5. Guinney J, Dienstmann R, Wang X, de Reyniès A, Schlicker A, Soneson C, et al. The consensus molecular subtypes of colorectal cancer. *Nat Med* 2015;**21**:1350−6.
6. Itatani Y, Yamamoto T, Zhong C, Molinolo AA, Ruppel J, Hegde P, et al. Suppressing neutrophil-dependent angiogenesis abrogates resistance to anti-VEGF antibody in a genetic model of colorectal cancer. *Proc Natl Acad Sci* 2020;**117**:21598−608.
7. Janes PW, Parslow AC, Cao D, Rigopoulos A, Lee F-T, Gong SJ, et al. An anti-VEGF-B antibody reduces abnormal tumor vasculature and enhances the effects of chemotherapy. *Cancers* 2024;**16**:1902.
8. Elebiyo TC, Rotimi D, Evbuomwan IO, Maimako RF, Iyobhebhe M, Ojo OA, et al. Reassessing vascular endothelial growth factor (VEGF) in anti-angiogenic cancer therapy. *Cancer Res Treat* 2022;**32**:100620.
9. Chen Z, Han F, Du Y, Shi H, Zhou W. Hypoxic microenvironment in cancer: molecular mechanisms and therapeutic interventions. *Signal Transduct Targeted Ther* 2023;**8**:70.
10. Emami Nejad A, Najafgholian S, Rostami A, Sistani A, Shojaeifar S, Esparvarinha M, et al. The role of hypoxia in the tumor microenvironment and development of cancer stem cell: a novel approach to developing treatment. *Cancer Cell Int* 2021;**21**:62.
11. Huang Y, Yuan J, Righi E, Kamoun WS, Ancukiewicz M, Nezivar J, et al. Vascular normalizing doses of antiangiogenic treatment reprogram the immunosuppressive tumor microenvironment and enhance immunotherapy. *Proc Natl Acad Sci* 2012;**109**:17561−6.
12. Du Four S, Maenhout SK, Niclou SP, Thielemans K, Neyns B, Aerts JL. Combined VEGFR and CTLA-4 blockade increases the antigen-presenting function of intratumoral DCs and reduces the suppressive capacity of intratumoral MDSCs. *Am J Cancer Res* 2016;**6**:2514−31.
13. Noman MZ, Desantis G, Janji B, Hasmim M, Karray S, Dessen P, et al. PD-L1 is a novel direct target of HIF-1α, and its blockade under hypoxia enhanced MDSC-mediated T cell activation. *J Exp Med* 2014;**211**:781−90.
14. Choi Y, Jung K. Normalization of the tumor microenvironment by harnessing vascular and immune modulation to achieve enhanced cancer therapy. *Exp Mol Med* 2023;**55**:2308−19.
15. Liu Z, Zhao Q, Zheng Z, Liu S, Meng L, Dong L, et al. Vascular normalization in immunotherapy: a promising mechanisms combined with radiotherapy. *Biomed Pharmacother* 2021;**139**:111607.
16. Liu J, Liu ZX, Wu QN, Lu YX, Wong CW, Miao L, et al. Long noncoding RNA AGPG regulates PFKFB3-mediated tumor glycolytic reprogramming. *Nat Commun* 2020;**11**:1507.
17. Chen ZX, Liu MD, Zhang MK, Wang SB, Xu L, Li CX, et al. Interfering with lactate-fueled respiration for enhanced photodynamic tumor therapy by a porphyrinic MOF nanoplatform. *Adv Funct Mater* 2018;**28**:1803498.
18. Gao F, Tang Y, Liu WL, Zou MZ, Huang C, Liu CJ, et al. Intra/-extracellular lactic acid exhaustion for synergistic metabolic therapy and immunotherapy of tumors. *Adv Mater* 2019;**31**:1904639.
19. Yuan P, Yang T, Mu J, Zhao J, Yang Y, Yan Z, et al. Circadian clock gene NPAS2 promotes reprogramming of glucose metabolism in hepatocellular carcinoma cells. *Cancer Lett* 2020;**469**:498−509.
20. Luo Y, Li Y, Huang Z, Li X, Wang Y, Hou J, et al. A nanounit strategy disrupts energy metabolism and alleviates immunosuppression for cancer therapy. *Nano Lett* 2022;**22**:6418−27.
21. Wang Y, Liao J, Lyu Y, Guo Q, Zhu Z, Wu X, et al. An AIE photosensitizer with simultaneous type I and type II ROS generation: efficient bacterial elimination and hypoxic tumor ablation. *Adv Funct Mater* 2023;**33**:2301692.
22. Zhang Y, Jia Q, Nan F, Wang J, Liang K, Li J, et al. Carbon dots nanophotosensitizers with tunable reactive oxygen species generation for mitochondrion-targeted type I/II photodynamic therapy. *Biomaterials* 2023;**293**:121953.
23. Li Z, Di C, Li S, Yang X, Nie G. Smart nanotherapeutic targeting of tumor vasculature. *Acc Chem Res* 2019;**52**:2703−12.
24. Qu C, Yuan H, Tian M, Zhang X, Xia P, Shi G, et al. Precise photodynamic therapy by midkine nanobody-engineered nanoparticles remodels the microenvironment of pancreatic ductal adenocarcinoma and potentiates the immunotherapy. *ACS Nano* 2024;**18**:4019−37.
25. Kim SJ, Jung KH, Son MK, Park JH, Yan HH, Fang Z, et al. Tumor vessel normalization by the PI3K inhibitor HS-173 enhances drug delivery. *Cancer Lett* 2017;**403**:339−53.
26. Liu S, Wang B, Yu Y, Liu Y, Zhuang Z, Zhao Z, et al. Cationization-enhanced type I and type II ROS generation for photodynamic treatment of drug-resistant bacteria. *ACS Nano* 2022;**16**:9130−41.
27. Deng H, Zhou Z, Yang W, Lin LS, Wang S, Niu G, et al. Endoplasmic reticulum targeting to amplify immunogenic cell death for cancer immunotherapy. *Nano Lett* 2020;**20**:1928−33.
28. Yuan H, Ma J, Huang W, Gong P, Shi F, Xu X, et al. Antitumor effects of a distinct sonodynamic nanosystem through enhanced induction of immunogenic cell death and ferroptosis with modulation of tumor microenvironment. *JACS Au* 2023;**3**:1507−20.
29. Yuan H, Xia P, Sun X, Ma J, Xu X, Fu C, et al. Photothermal nanozymatic nanoparticles induce ferroptosis and apoptosis through tumor microenvironment manipulation for cancer therapy. *Small* 2022;**18**:2202161.
30. Zhou F, Feng B, Yu H, Wang D, Wang T, Ma Y, et al. Tumor microenvironment-activatable prodrug vesicles for nanoenabled cancer chemoimmunotherapy combining immunogenic cell death induction and CD47 blockade. *Adv Mater* 2019;**31**:1805888.
31. Wu W, Pu Y, Zhou B, Shen Y, Gao S, Zhou M, et al. Photoactivatable immunostimulatory nanomedicine for immunometabolic cancer therapy. *J Am Chem Soc* 2022;**144**:19038−50.
32. Yang C, Wang M, Chang M, Yuan M, Zhang W, Tan J, et al. Heterostructural nanoadjuvant CuSe/CoSe2 for potentiating ferroptosis and photoimmunotherapy through intratumoral blocked lactate efflux. *J Am Chem Soc* 2023;**145**:7205−17.
33. Chen N, Hao C, Peng X, Lin H, Yin A, Hao L, et al. Roxadustat for anemia in patients with kidney disease not receiving dialysis. *N Engl J Med* 2019;**381**:1001−10.
34. Choi Y, Son W, Han Y, Chae J, Yang CS, Choi J. Glycan targeting nanoparticle for photodynamic immunotherapy of melanoma. *Acta Pharm Sin B* 2023;**13**:1903−18.
35. Chen C, Song M, Du Y, Yu Y, Li C, Han Y, et al. Tumor-associated-macrophage-membrane-coated nanoparticles for improved photodynamic immunotherapy. *Nano Lett* 2021;**21**:5522−31.
36. Wan J, Zhang X, Tang D, Liu T, Xiao H. Biodegradable NIR-II pseudo conjugate polymeric nanoparticles amplify photodynamic immunotherapy *via* alleviation of tumor hypoxia and tumor-associated macrophage reprogramming. *Adv Mater* 2023;**35**:2209799.
37. Lu Q, Kou D, Lou S, Ashrafizadeh M, Aref AR, Canadas I, et al. Nanoparticles in tumor microenvironment remodeling and cancer immunotherapy. *J Hematol Oncol* 2024;**17**:16.
38. Jiang H, Fu H, Guo Y, Hu P, Shi J. Evoking tumor associated macrophages by mitochondria-targeted magnetothermal immunogenic cell death for cancer immunotherapy. *Biomaterials* 2022;**289**:121799.